EFDA–JET–CP(10)08/49

P. Buratti, M. Baruzzo, R.J. Buttery, C.D. Challis, I.T. Chapman, F. Crisanti,
L. Figini, M. Gryaznevich, T.C. Hender, D.F. Howell, H. Han, E. Joffrin,
J. Hobirk, F. Imbeaux, O.J. Kwon, X. Litaudon, J.Mailloux
and JET-EFDA contributors

Kink Instabilities in High-Beta JET Advanced Scenarios

Kink Instabilities in High-Beta JET Advanced Scenarios

P. Buratti[1], M. Baruzzo[2], R.J. Buttery[3], C.D. Challis[4], I.T. Chapman[4], F. Crisanti[1], L. Figini[5], M. Gryaznevich[4], T.C. Hender[4], D.F. Howell[4], H. Han[6], E. Joffrin[7], J. Hobirk[8], F. Imbeaux[7], O.J. Kwon[9], X. Litaudon[7], J.Mailloux[4]
and JET-EFDA contributors*

JET-EFDA, Culham Science Centre, OX14 3DB, Abingdon, UK

[1]EURATOM-ENEA Fusion Association, C.R. Frascati, CP65, 00044 Frascati, Italy
[2]Consorzio RFX, EURATOM-ENEA Association, Corso Stati Uniti 4, 35127 Padova, Italy
[3]General Atomics, San Diego, CA, USA
[4]EURATOM-CCFE Fusion Association, Culham Science Centre, OX14 3DB, Abingdon, OXON, UK
[5]Istituto di Fisica del Plasma, Associazione EURATOM ENEA -CNR,Milano, Italy
[6]Department of Nuclear Engineering, Seoul National University, Seoul 151-742 Korea
[7]CEA, IRFM, F-13108 Saint Paul-lez-Durance, France
[8]Max-Planck-Institut für Plasmaphysik, Garching, Germany, Euratom Assoziation
[9]Department of Physics, Daegu University, Gyeongbuk 712-714 Korea
** See annex of F. Romanelli et al, "Overview of JET Results",*
(23rd IAEA Fusion Energy Conference, Daejon, Republic of Korea (2010)).

Preprint of Paper to be submitted for publication in Proceedings of the
23rd IAEA Fusion Energy Conference, Daejon, Republic of Korea
(10th October 2010 - 16th October 2010)

ABSTRACT.
Stability of high-beta plasmas is studied on discharges from a series of JET experiments on steady-state and hybrid advanced scenarios, with a wide range of q-profiles and a range of normalized beta extending to $\beta_N = 4$. Bursting and continuous forms of global $n = 1$ instabilities limit the achievable β_N or degrade confinement. Stability boundaries in terms of q_{min} and pressure peaking are determined. For relatively broad pressure profiles the limit decreases from $\beta_N = 4$ at $q_{min} = 1$ to $\beta_N = 2$ at $q_{min} = 3$, while at fixed q_{min} it decreases with increasing pressure peaking. Triggering mechanisms and the internal structure of continuous $n = 1$ instabilities are analysed. A new form of instability that grows on typical resistive time-scales but has internal kink structure is identified.

1. INTRODUCTION

Stability at high plasma pressure is an important issue for advanced tokamak scenarios that aim at steady-state or long pulse reactor operation. A convenient measure of plasma pressure is the normalized plasma beta, defined as $\beta_N = \beta /(I_p /aB)$, where β is the ratio of plasma pressure to magnetic field pressure and the combination of plasma current I_p, minor radius a and toroidal magnetic field B at the denominator accounts for the existence of an unfavorable curvature region on the Low-Field-Side (LFS) of the torus. The two main candidate scenarios for advanced tokamak operation are the steady-state scenario, which aims at fully non-inductive operation and the hybrid scenario, which aims at lowering flux consumption for long pulse operation. Both scenarios require the achievement of reliable operation at $\beta_N \approx 3$ for efficient reactor operation. This requirement is particularly challenging for the steady-state scenario, which relies on broad current profiles and peaked pressure profiles in order to maximize the bootstrap current contribution, since both conditions tend to lower the critical β_N for the onset of pressure-driven global instabilities. Kink modes and Resistive Wall Modes (RWM, a wall-stabilised branch of the kink mode that grows on the time scale of current diffusion in the wall), have been reported as disruptive beta-limiting instabilities in several discharges with strong pressure peaking [1]. In addition, chirping modes thought to be driven by energetic particles (and for this reason dubbed "$q = 2$ fishbones" by some authors) were found in JET, DIII-D and JT-60U near the beta limit [2-4]. Another global mode, the neoclassical tearing mode (NTM) with poloidal/toroidal periodicity $m/n = 2/1$, has been reported as a performance limiting instability at high beta [5, 6].

High-beta conditions have been explored in experiments on steady-state and hybrid advanced scenarios in JET [7-10]. The database collected from these experiments in order to study the beta limits is described in Section 2. A survey on the observed high-beta instabilities is given in Section 3 and the influence of current density and pressure profiles on their onset is discussed in Section 4. The characteristics of high-beta instabilities are analysed in Section 5.

2. High beta scenarios in JET

In recent 2008-2009 experimental campaigns, JET has performed a systematic development of steady state [8] and hybrid advanced scenarios [7, 10], including a series of experiments specifically dedicated to exploration of the beta limit [9]. A database with more than 500 cases has been assembled from discharges performed for these experiments. The explored range of normalized beta extends up to $\beta_N = 4$, while q_{95} and varies from 3.5 to 5.5 and $q_{\min}$ from MSE varies from 0.73 to 2.9. Included discharges from the steady-state scenario are at B/I_p = 2.7/1.8 or 2.3/1.5, the ones from dedicated beta limit experiments are at 1.8/1.2 and hybrid ones at 1.7/1.4, 2/1.7 and 2.4/2. Most have high-triangularity shapes ($\delta \approx 0.4$), with a subset of hybrid discharges at $\delta \approx 0.2$. All the discharges are in H-mode with type-I ELMs.

3. BETA-LIMITING INSTABILITIES

The ultimate beta-limiting instabilities observed throughout the database are global n = 1 modes that appear in busting or in continuous forms. The bursting form, which is found in discharges of the steady-state scenario, can give rise to a fast beta collapse or to a disruption. The continuous form is found both in hybrid and in steady-state regimes; in the latter, it is the main obstacle to the prolongation of high β_N phases at high confinement. The same instability is not a major problem in the hybrid scenario, but inclusion of discharges from this scenario in the database allows extending the stability study to a wide range of q-profile shapes. In many cases the continuous mode has kink structure during its growth, i.e. it displaces flux surfaces without forming any magnetic island (see Sect.5.2). Figure 1 shows all types of n = 1 activities observed throughout the database, excepting fishbones and sawtooth precursors that are present in hybrid discharges. Besides the mentioned bursting and continuous modes, a broadband activity is present near the top frequency of bursting modes; this is not really a beta-limiting one, rather it is a marker of proximity to the onset of bursting modes.

A range of tearing modes with $n \leq 6$ is present in several cases, particularly in the hybrid regime. Tearing modes with $2 \leq n \leq 3$ provoke a serious (20-40%) degradation of confinement, but a safe route with respect to these modes has been identified in terms of q-profiles [7, 10].

In the following attention will be focused on $n = 1$ modes. Fig.2 shows the variation of confinement due to the n = 1 activities for the case shown in Fig.1. The broadband activity has no effect on confinement. Bursting modes are relatively weak in this case and have a small effect on global quantities, the energy content decreases by 5% or less at each burst and recovers well before the next one. The continuous mode has relevant effects; after its onset, the normalized beta decreases from 2.55 to 1.5 at constant heating power, while the confinement enhancement factor with respect to the IPB98(y,2) scaling drops from 1.3 to 0.8.

4. EFFECTS OF CURRENT DENSITY AND PRESSURE PROFILES

The achieved β_N values at continuous mode onset are affected by the qmin value, as shown by the red stars in Fig.3. Top values form a clear boundary that decreases from $\beta_N = 4$ at $q_{\min} \approx 1$ to $\beta_N = 2$ at $q_{\min} \approx 3$; there is moreover a “dip” at $q_{\min} \approx 2$ with some unstable points at $\beta_N < 1.5$. If q0 is used instead of $q_{\min}$, top values remain ordered but the dip spreads out between 2 and 3. No correlation is found with the internal inductance (which varies between 0.6 and 0.8), however it is interesting to note that the top β_N values vary between 5.4li at $q_{\min} \approx 1$ and 3.4li at $q_{\min} \approx 3$. Figure 4 illustrates trajectories of three discharges in the same diagram; red segments show the interval of the MSE time grid during which the continuous mode starts. Each trajectory is stopped after mode onset. MISHKA code calculations along the trajectories give no-wall ideal instability slightly before the mode onset for each discharge; the case at higher β_N is also unstable with wall at 1.1 normalised radius. Figure 3 also shows the maximum β_N in discharges without any n = 1 mode (blue dots), the maximum bN during broadband n = 1 activity (green squares), β_N during cycles of bursting n = 1 modes (yellow triangles) and β_N just before disruptions initiated by a bursting mode (black triangles). Broadband and bursting modes are distributed in two adjacent horizontal bands. Continuous modes have a sharp upper boundary but are otherwise scattered across the diagram. This can be partly understood by analyzing trigger events. Besides the well-known sawtooth crash and ELM trigger events, there are cases in which the $n = 1$ mode starts as a sub harmonic of a pre-existing $m/n = 5/2$ tearing mode (Fig.5). Spontaneous modes are identified when the onset is well separated from any ELM or sawtooth event; an example is shown in Fig.6.

Figure 7 shows the distribution of trigger types in the operational diagram. Modes starting at lower β_N for each $q_{\min}$ are triggered by sawtooth crashes or by the $m/n = 5/2$ mode, with the exception of the $q_{\min} \approx 2$ region that can be unstable to spontaneous modes at low β_N. Excluding this region, the beta limit appears as a transversal belt populated by spontaneous modes. The width of this belt at fixed $q_{\min}$ and the fact that disruptions do not occur at the top β_N values can be related to the different pressure profile shapes that are present in the database. This is illustrated by Fig.8, in which ion temperature profiles at the latest time before instability are shown for three discharges at $q_{\min} \approx 1.5$: the one with broader profile achieves $\beta_N = 3.3$, while the two ones that have more peaked profiles (due to internal transport barriers) develop the continuous mode or disrupt at $\beta_N = 2.6$ and at $\beta_N = 2.35$ respectively. This empirical "operational diagram" approach can not be probably pushed beyond this point, in fact stability should depend on the alignment between pressure gradient and integer-q surfaces, which can not be represented by a single operational parameter. Stability boundaries calculated by the MISHKA code following profiles evolution in a real discharge are shown in Fig.9. At each time, $q_{\min}$ and the poloidal beta β_p have been varied independently at fixed pressure and current density normalized profiles. The obtained moving boundary is shown by a series of lines with different colors. The actual discharge trajectory (shown by markers) crosses the stability boundary at $t = 5.9$s. Bursting and continuous modes are observed in this discharge at $t = 6$s and at $t = 6.29$s respectively.

5. CHARACTERISTICS OF BETA-LIMITING INSTABILITIES

Useful information on drive and saturation mechanisms of beta-limiting instabilities can be gained by analyzing their structure and dynamics. Bursting and continuous modes are treated separately as the former require time-domain analysis, while the latter can be analysed by means of Fourier techniques.

5.1. BURSTING N = 1 MODES

Bursting modes (indicated by yellow and black triangles in Fig.4) typically grow in a few ms and chirp-down in frequency by 25%. They closely resemble the ones reported in [2, 3, 4]. After the initial growth, these modes can either saturate and decay, or trigger an ELM (in some cases a giant one with 1 MJ energy loss), or end up in a major disruption. The raw magnetic signals for three such cases are shown in Fig.10. During the first 2ms the growth is exponential and amplitude is nearly the same in all cases; after that in one case signal saturates and decays (green trace in Fig. 10), while in the others the growth rate suddenly increases. Frequency evolution of bursting modes resembles the one of ordinary $q = 1$ fishbones that are present in many hybrid discharges of the database, but a direct comparison reveals important differences. In particular, $q = 1$ fishbones are localised near the plasma center and do not affect the plasma energy content; on the contrary, $q_{min} > 1$ bursting modes are global, with peak displacement around mid radius, and can result in an important loss of plasma energy. Also amplitude evolution is different: $q = 1$ fishbones grow exponentially at first and smoothly saturate, while $q_{min} > 1$ bursting modes can have super-exponential growth and seldom saturate without triggering a profile rearrangement.

5.2. THE CONTINUOUS N = 1 MODE

Continuous $n = 1$ modes appear in about 33% of the discharges included in the database. Mode frequencies (4-14 kHz throughout the database) correspond to plasma rotation at $q = 2$ (this happens in most cases) or at $q = 3$. In some instances modes corresponding to $q = 2$ and $q = 3$ coexist. Growth times are extremely variable, ranging from 2ms to hundreds of ms. Once triggered, continuous modes persist up to the end of main heating or beyond. Mode locking, possibly leading to disruptions, occurs in a few cases (this kind of disruption is not included in Fig. 3, which only concerns the onset of continuous modes).

Long-lasting, beta-limiting modes in advanced scenarios were previously identified as $m/n = 2/1$ neoclassical tearing modes [5, 6], which can grow only if a sufficiently large magnetic island is present. In contrast, continuous modes that grow in the absence of a magnetic island and then require a different drive can be found in JET. Magnetic islands are detected by radial analysis of temperature oscillations. An island is associated with a π-jump of phase and a zero of amplitude at the island radius. Phase and amplitude information is extracted from radial cross-spectral analysis of 48 ECE channels with fast (250kHz) data acquisition. For each ECE channel (k), the signal is segmented into a sequence of 50% overlapped data blocks. For each block the cross-spectral density G_{kM} (f) with a reference magnetic signal (M) is calculated on $N = 8$ sub block samples and averaged. The phase angle of G_{kM} at the mode frequency gives phase ϕ_k. Data for all channels are stored in the phase map ϕ (R, t) where R and t vectors represent positions of ECE channels and central times of data blocks. Coherence and amplitude maps are constructed from $\gamma_{kM} = |G_{kM}|/\sqrt{G_{kk}\,G_{MM}}$ and $A_{kM} = |G_{kM}|/\sqrt{G_{MM}}$ respectively. Expected random errors (absolute on ϕ_k and relative on A_k) are $\sqrt{1-\gamma^2_{kM}} = |\gamma_{kM}|\sqrt{2N}$. Figure 11 shows phase and amplitude profiles for Pulse No: 77590 at $t = 6.7$s (160ms after mode start), when amplitude has reached 86% of the maximum value. This discharge has been selected for it has the highest quality ECE measurements, with the entire profile measured at the second ECE harmonic at the highest field (2.7T) in the database; ray-tracing calculations show that in this case the maximum deviation of the ECE sightline due to refraction is within 1 cm. The phase profile has a basic arctangent profile because the ECE sightline is below the plasma axis and then samples different poloidal angles. There is a phase jump on the HFS, at $R = 2.7$m, but no phase jump can be seen on the LFS. This profile can be explained by the presence of two non-reconnected mode components with $m = 2$ and $m = 3$ that are in phase on the LFS and consequently in opposition on the HFS: the phase jump occurs on the HFS where the $m = 3$ component goes over the $m = 2$ one. This picture is consistent with kink eigenfunctions calculated by the MISHKA code for this discharge. Fig. 12 shows profiles at $t = 6.7$s; at this time a clear phase jump accompanied by an amplitude dip appears on the LFS at $R = 3.51$ m. Still the mode structure is more complex than a simple tearing mode with a reconnected $m = 2$ component, in fact there is an extra phase jump at $R = 3.6$ m, which can be explained by the persistence of a non-reconnected $m = 3$ component [11]. During the kink-like stage the poloidal distribution of magnetic perturbation amplitudes at the in-vessel coils has strongly ballooning character, with LFS amplitudes one order of magnitude larger than HFS ones (see Fig.2c). The two amplitudes converge and the ballooning character progressively disappears as the continuous mode evolves from kink-like to tearing-like.

Application of radial analysis to all cases with available ECE fast windows shows that modes triggered by the 5/2 mode and spontaneous modes at low β_N and $q_{\mathrm{min}} \approx 2$ have tearing character from the beginning. In the other subgroups (sawtooth-triggered, ELM-triggered and spontaneous), tearing and kink cases are shuffled in the β_N - q_{min} diagram; the incidence of continuous modes with initial kink structure is about 65%, with a typical duration of the kink phase of 200ms.

5.3. COMPARISON WITH EIGENFUNCTIONS FROM THE MISHKA CODE

In order to check the multi-harmonic picture of the kink-like continuous mode, measured phase profile is compared with the one predicted by the MISHKA code, which calculates a spectrum of poloidal components of the plasma displacement ranging from $m = 0$ to $m = 20$. The phase of each component along the ECE sightline varies according to $m\theta(r)$, where θ is the local poloidal angle. Phase profiles are calculated after summing sine and cosine parts for all components. The ECE radial positions are shifted by 9 cm; this is necessary to have agreement with equilibrium, i.e. to force the HFS and LFS branches of the temperature profile to be a single flux function. Figure 13 shows measured (in red) and calculated (in blue) phase profiles, together with profiles corresponding to three pure poloidal components (dashed lines). There is a remarkable overall agreement, but the π-jump on the HFS is smoother for the calculated profile.

CONCLUSIONS

Stability of high-beta advanced scenarios in JET has been analysed for a wide range of q-profiles and normalized beta values up to $\beta_N = 4$. Global $n = 1$ instabilities limit the achievable β_N or degrade confinement. Stability boundaries in terms of q_{min} and pressure peaking have been determined. For relatively broad pressure profiles the limit decreases from $\beta_N = 4$ at $q_{min} = 1$ to $\beta_N = 2$ at $q_{min} = 3$, while at fixed q_{min} it decreases with increasing pressure peaking.

Bursting and continuous forms $n = 1$ instabilities have been analysed. A new form of instability that grows on typical resistive time-scales but has kink internal structure is identified. This instability systematically occurs above the no-wall ideal stability limit as calculated for $n = 1$ modes by the MISHKA code. The measured mode structure is in good agreement with eigenfunctions given by the code.

ACKNOWLEDGMENT.

This work was supported by EURATOM and carried out within the framework of the European Fusion Development Agreement. The views and opinions expressed herein do not necessarily reflect those of the European Commission.

REFERENCES

[1]. E.J. Strait, Fusion Science and Technology, **48** (2005) 864.

[2]. G.Huysmans et al., Nuclear Fusion **39** (1999) 1489.

[3]. M. Okabayashi et al., 2009 Nuclear Fusion **49** 125003.

[4]. G. Matsunaga et al., Physical Review Letters **103** (2009) 045001

[5]. A. Staebler et al., Nuclear Fusion **45** (2005) 617.

[6]. T.C. Luce et al., Physics of Plasmas **11** (2004) 2627.

[7]. J. Hobirk et al., 36thEPS Conference on Plasma Physics, ECA Vol. 33E (2009) O5.057

[8]. J. Mailloux et al., paper this Conference

[9]. C.D. Challis et al., 36thEPS Conference on Plasma Physics, ECA Vol. 33E (2009) P5.172

[10]. E. Joffrin et al., paper this Conference

[11]. M. Baruzzo et al., Plasma Physics and Controlled Fusion **52** (2010) 075001

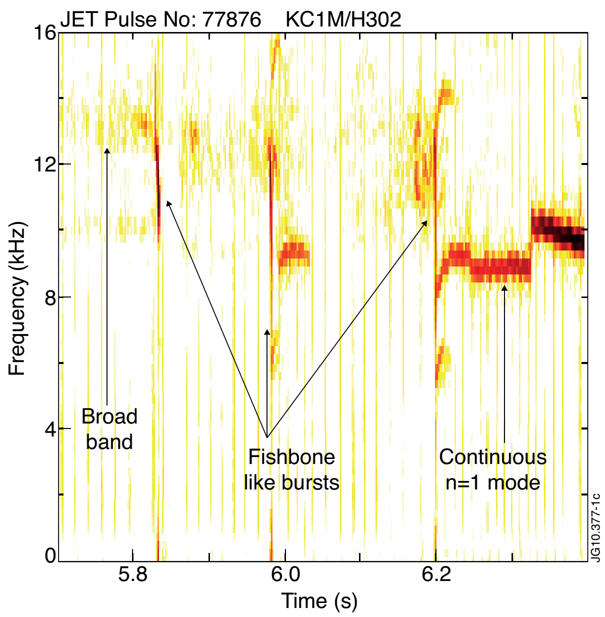

Figure 1: Spectrogram of a magnetic coil signalin a steady-state scenario. Color intensity represents log amplitude.

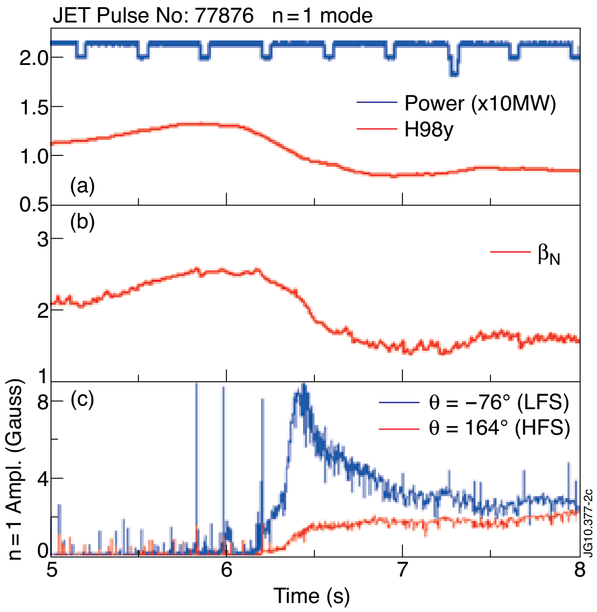

Figure 2: a) Power and confinement factor waveforms. b) Normalized beta. c) n=1 mode amplitude on LFS (blue) and HFS (red); fishbone-like events appear as spikes. The tearing-like stage starts at t =6.45s.

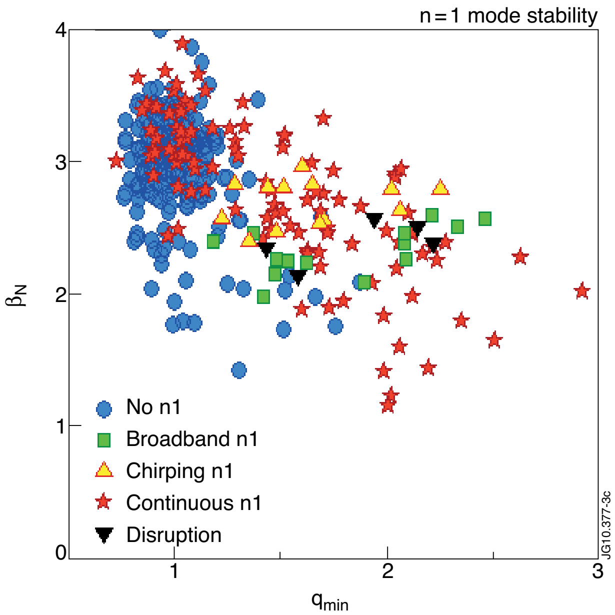

Figure 3: Operational stability diagram. Blue dots and green squares respectively indicate maximum β_N in discharges without n = 1 modes and with broadband activity only. Yellow triangles and red stars show β_N values at the onset of bursting an continuous n = 1 modes respectively. Black triangles indicate disruptions.

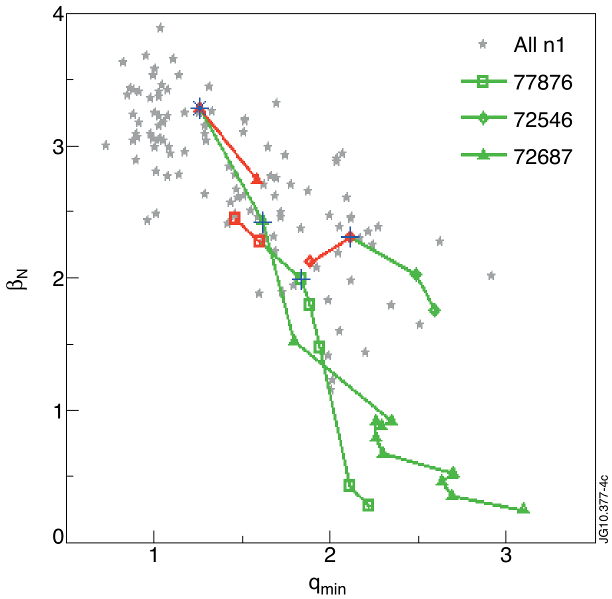

Figure 4: Trajectories in the operational diagram. Onset of the n = 1 mode occurs at some point of the red segments. Grey stars represent all onsets. Crosses and asterisk mark the onset of no-wall and with-wall ideal instability conditions from the MISHKA code.

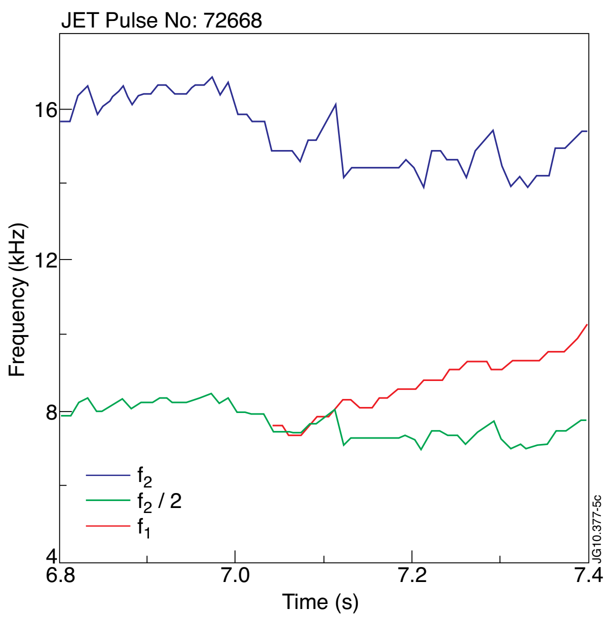

Figure 5: n=2 (f_2, blue) and n=1 (f_1, red) mode frequencies. f_1 starts at $f_{2/2}$ (green).

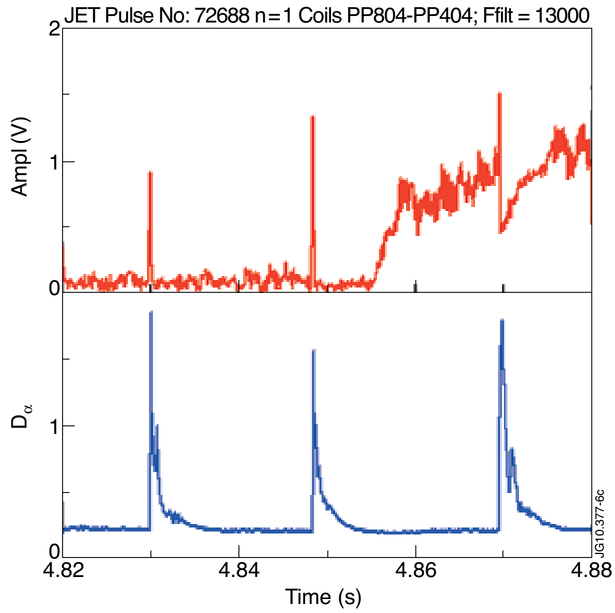

Figure 6: Magnetic and D_α signals. Mode onset at t=4.855 is far from ELMs. No sawteeth are present.

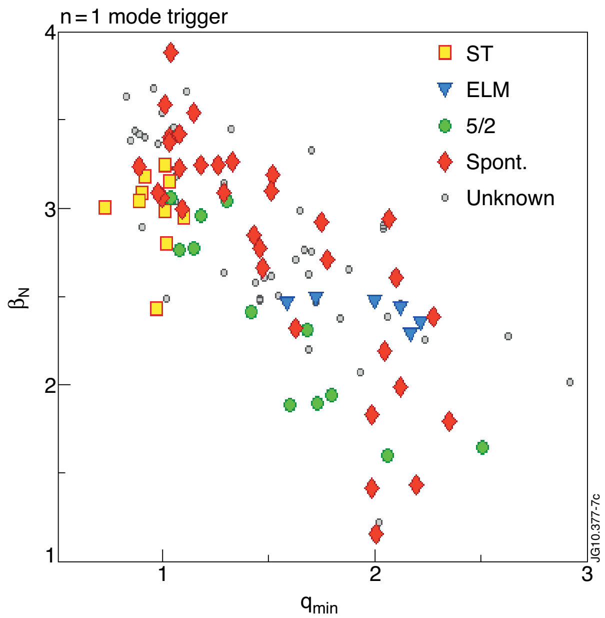

Figure 7: Types of continuous mode onset. Squares, circles and triangles indicate triggering by sawtooth, ELM and 5/2 mode respectively. Diamonds correspond to spontaneous modes and dots to uncertain cases.

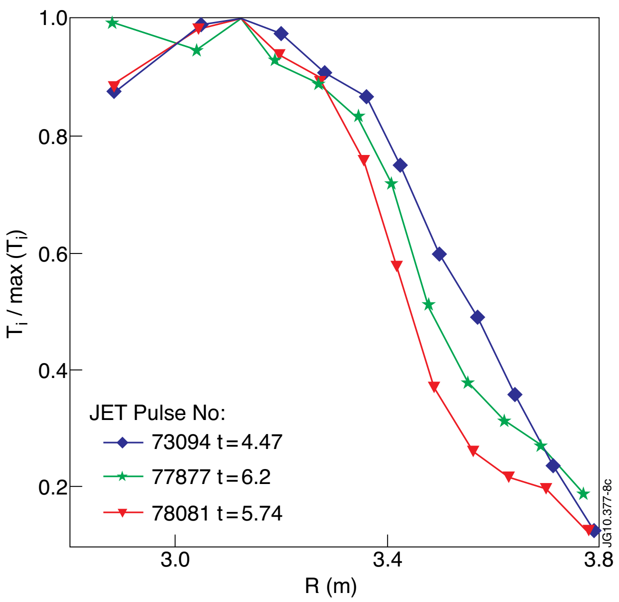

Figure 8: Normalised ion temperature profiles at $q_{min} \approx 1.5$. Pulse No: 73094 develops the continuous mode at $\beta_N = 3.3$; 77877 shows mild bursting modes and then the continuous mode at $\beta_N = 2.6$; 78081 has a disruptive bursting mode at $\beta_N = 2.35$.

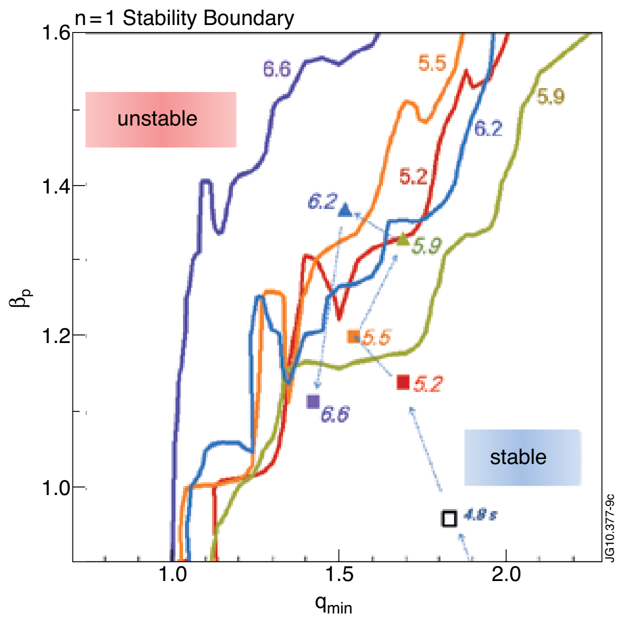

Figure 9: Stability boundaries for Pulse No: 77877. Lines in different colors correspond to different times. The experimental trajectory is shown by markers (triangles fall in the unstable region) following the time/color coding. This discharge has bursting modes at t = 6s and the continuous mode at t = 6.29s.

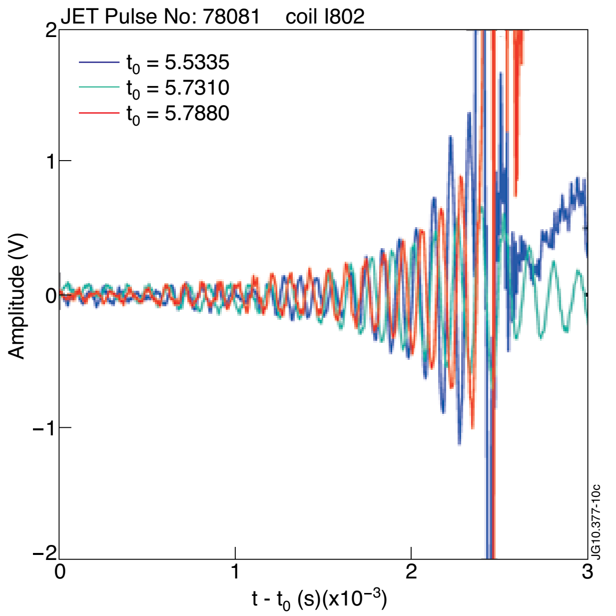

Figure 10: Magnetic signal during bursting modes, overlaid by time-shift. The case in green saturates with a small ELM and decays; the one in blue ends with a giant ELM, the one in red results in a disruption.

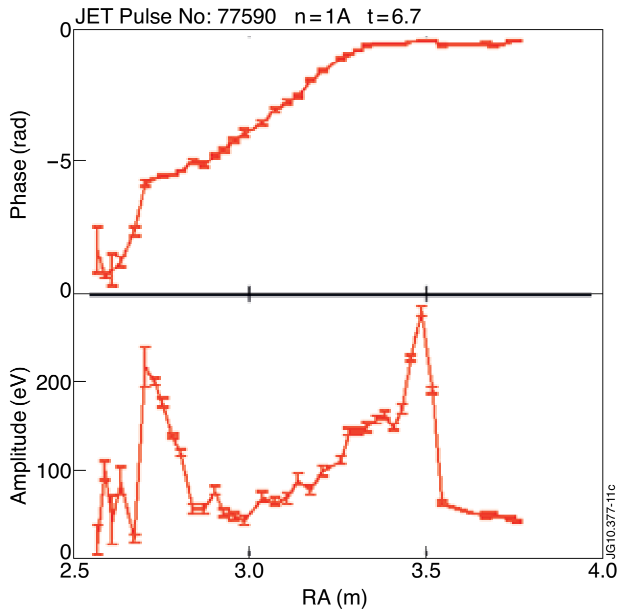

Figure 11: Phase and zero-to-peak amplitude profiles along the major radius on the ECE sightline during the kink-like stage of the continuous mode, with the distinctive feature of smooth phase profile on the LFS. The slope around the plasma center(R = 3.1 m) is due to the fact that the ECE sightline samples different poloidal angles.

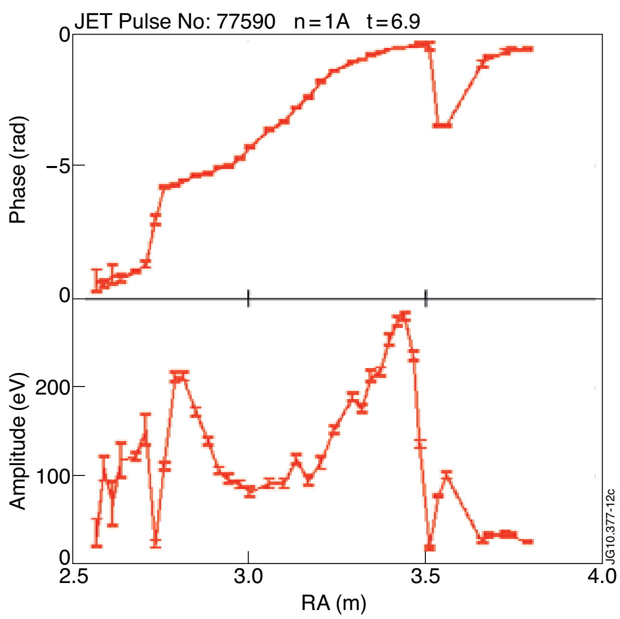

Figure 12: Phase and amplitude profiles along the major radius on the ECE sightline during the tearing-like stage of the continuous mode, with a clear p-jump of phase and a dip of amplitude on the LFS.

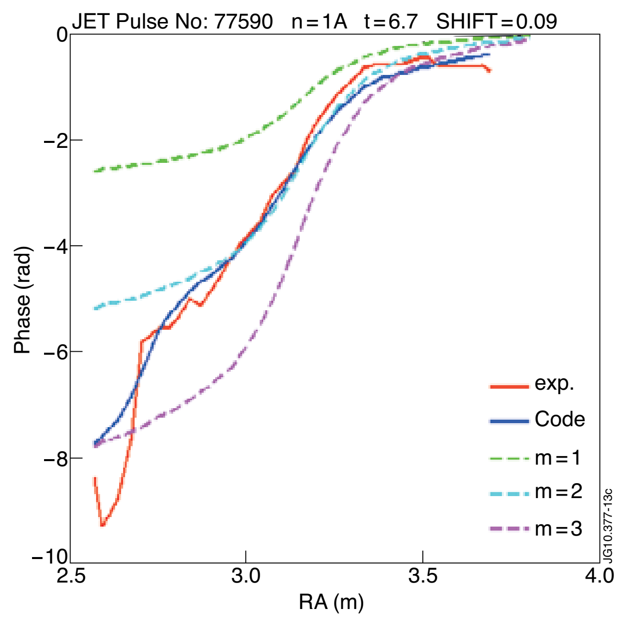

Figure 13: Measured (red) and calculated (blue) phase profiles along the ECE sightline. Dashed lines show profiles for pure poloidal components.